Stability and rupture of bifurcation bridges in semiconductor lasers subject to optical feedback

B. Haegeman,* K. Engelborghs, and D. Roose
Department of Computer Science, K.U. Leuven, Celestijnenlaan 200A, 3001 Heverlee, Belgium

D. Pieroux and T. Erneux
Optique Nonlinéaire Théorique, Université Libre de Bruxelles, Campus Plaine, Code Postal 231, 1050 Bruxelles, Belgium
(Received 26 April 2002; published 24 October 2002)

The bifurcation diagram of a single-mode semiconductor laser subject to a delayed optical feedback is examined by using numerical continuation methods. For this, we show how to cope with the special symmetry properties of the equations. As the feedback strength is increased, branches of modes and antimodes appear, and we have found that pairs of modes and antimodes are connected by closed branches of periodic solutions (bifurcation bridges). Such connections seem generically present as new pairs of modes and antimodes appear. We subsequently investigate the behavior of the first connection as a function of the linewidth enhancement factor and the feedback phase. Our results extend and confirm existing results and hypotheses reported in the literature. For large values of the linewidth enhancement factor ($\alpha = 5$–6), bridges break through homoclinic orbits. Changing the feedback phase unfolds the bifurcation diagram of the modes and antimodes, allowing different types of connections between modes.

DOI: 10.1103/PhysRevE.66.046216 PACS number(s): 42.60.Mi, 42.55.Px

I. INTRODUCTION

Semiconductor lasers with a long external cavity are very sensitive to external signals. The light traveling back and forth in the external cavity takes a long time relative to the internal time scale of the laser, and produces a delayed interaction with a large delay. Because of the large delay, a small amount of optical feedback is enough to produce a variety of instabilities [1–4]. When the laser is pumped just above threshold, intensity dropouts occur irregularly. This phenomenon, called low-frequency fluctuations (LFF), has been intensively studied during the last decade [5,6]. For lasers with a short external cavity and for cleaved-coupled-cavity lasers, instabilities prevail if the feedback is sufficiently strong [7–9].

A minimal description of a single-mode semiconductor laser exposed to weak optical feedback was proposed by Lang and Kobayashi (LK) [10]. In dimensionless form, the LK equations consist of two rate equations for the complex electrical field $E(t)$ and the excess carrier number $N(t)$. They are given by [11]

$$\frac{dE}{dt} = (1+i\alpha)NE + \kappa \exp(-i\omega_0\tau)E(t-\tau),$$

$$T\frac{dN}{dt} = P - N - (1+2N)|E|^2. \tag{1}$$

In these equations, time t is measured in units of the photon lifetime τ_p ($\tau_p \simeq 1$ps). T and τ are the carrier lifetime and the external round-trip time, respectively, normalized by τ_p ($T \simeq 1000$, $\tau \simeq 1000$). ω_0 is the dimensionless frequency of the solitary laser, κ is the feedback strength ($0 \leqslant \kappa \ll 1$), P is the pump current above threshold ($|P| < 1$), and α is the linewidth enhancement factor.

The LK equations are delay differential equations (DDEs), because the right-hand side of Eq. (1) does not only depend on $E(t)$ and $N(t)$ at the present time, but also on $E(t-\tau)$. Moreover, in the LK problem, the delay τ is large and should be taken into account explicitly. The state space of DDEs is infinite dimensional. This complicates and limits the theoretical understanding of the mathematical model. Analytical calculation of the first Hopf bifurcation, for example, already leads to complicated mathematics [12]. Most existing numerical investigations consist of simulations (time integration) that are time consuming and only reveal the stable solutions [9,13]. They do not allow two-parameter studies. The first objective of this paper is to describe a different numerical strategy in order to follow particular features of the bifurcation diagram.

Hohl and Gavrielides [13] investigated both experimentally and numerically how LFF appears as the result of cascading bifurcations from external cavity modes (ECMs). The ECMs are periodic solutions of Eq. (1) exhibiting a constant intensity, and they sequentially appear as the feedback strength κ is increased. In the presence of a small number of ECMs, they observed a series of bifurcations between the destabilization of one ECM and the appearance of the next stable one, which eventually leads to irregular behavior with a broad spectrum and chaotic time traces. They showed how this irregular behavior gradually evolves into LFF for larger values of κ (and thus more destabilized ECMs).

The bifurcation diagram in Ref. [13] was based on simulations of the LK equations in order to detect stable ECMs and their bifurcations. In Ref. [14], we reviewed this bifurcation diagram by using a continuation method. We discovered that Hopf bifurcation branches (bridges) are connecting the isolated ECMs. Physically, these bridges correspond to

*Electronic address: bart.haegeman@fys.kuleuven.ac.be

the beating of two nearby ECMs and seem to appear for every pair of ECMs. How robust are these bridges as we vary the laser fixed parameters? Are other connections between modes possible? The second objective of this paper is to examine the behavior of these bridges by two parameter studies. Specifically, we propose a detailed numerical bifurcation analysis of the LK equations, using DDE-BIFTOOL [15,17]. This MATLAB software package calculates steady state and periodic solutions for equations with a finite number of fixed discrete delays. Stability analysis of steady state solutions is achieved through approximating and correcting the rightmost characteristic roots [18]. Periodic solutions are computed using piecewise polynomial collocation and adaptive mesh selection [16]. Stability of periodic solutions is determined by computing approximations to the Floquet multipliers. Having access to both stable and unstable solutions, the behavior of the bifurcation bridges can be described. The LK equations exhibit a rotational symmetry that needs to be exploited to calculate the phenomena of interest. This important point is explained in the following section.

Asymptotic approximations of the bridges are possible by analyzing the large T limit of the LK equations [19]. Analytical expressions for the amplitude of the solutions in terms of the laser fixed parameters are thus available. They motivate new numerical bifurcation studies on how bridges change in terms of the laser fixed parameters. We choose the linewidth enhancement factor α and the feedback phase $(\omega_0\tau)$ mod (2π). The linewidth enhancement factor α is a laser material property that depends on the semiconductor laser. It has a definite effect on the stability of the periodic solutions as demonstrated experimentally in Refs. [20,21]. The feedback phase $(\omega_0\tau)$ mod(2π) is a key parameter for stability diagrams. Varying the position of the external mirror over one half optical wavelength (250–750 nm) causes a variation in the phase $(\omega_0\tau)$ mod (2π) over its full range $[0,2\pi]$. However, this variation does not significantly modify the external round-trip time τ itself, and the feedback phase $(\omega_0\tau)$ mod (2π) is generally regarded as an independent parameter. We may also control the feedback phase by changing the pump, as in Ref. [22]. In the rest of the paper, we will use the notation $\omega_0\tau$ instead of $(\omega_0\tau)$ mod (2π). We will be particularly interested in the stability of the bifurcation bridges. As we shall demonstrate, rupture may occur either through the appearance of homoclinic orbits or by unfolding the diagram of the ECMs.

The continuation methods of DDE-BIFTOOL have been recently used for other laser problems that we briefly review. Sciamanna *et al.* [23,24] examined the response of vertical-cavity surface-emitting lasers (VCSELs) subject to optical feedback. VCSELs are semiconductor lasers exhibiting two polarizations. The laser rate equations are more complicated than Eq. (1), but the bifurcation diagram reveals bifurcation bridges between modes similar to the one observed for the regular LK problem. It also motivated a new bifurcation analysis of Eq. (1) for low values of α [25]. A reduction of Eq. (1) where the carrier density N is adiabatically eliminated is examined by Pieroux and Mandel in Ref. [26]. Bifurcation bridges connecting modes are still observed. Green and Krauskopf studied the bifurcation diagram of a laser subject to phase conjugated feedback [27,28]. There is one phase and frequency locked solution. Branches of pulsating intensity solutions are, however, possible.

The paper is organized as follows. In Sec. II, we describe how we performed the numerical computations, exploiting the rotational symmetry of the LK equations (1). This section is not needed for the comprehension of the bifurcation diagrams. Section III confirms and extends the results of Ref. [13] where extensive simulations were used to analyze bifurcations with respect to the feedback strength κ. In Secs. IV and V, we investigate the dependence on the linewidth enhancement factor α and the feedback phase $\omega_0\tau$, respectively. Section VI summarizes our main observations.

II. EXPLOITING SYMMETRY

The LK equations (1) exhibit a rotational symmetry, see, e.g., Ref. [29], which can be exploited. Indeed, for every solution $(E(t),N(t))$, the pair $(E(t)\exp(i\phi),N(t))$ with $0 \leqslant \phi \leqslant 2\pi$ is a solution as well. The phase ϕ has no physical meaning. Hence, solutions with different ϕ can be considered as different members of one family of solutions. We call this the ϕ indeterminacy. This symmetry has important analytical and numerical consequences.

In order to study external cavity modes, which are single-frequency periodic solutions of Eq. (1), and their bifurcations, we transform the original autonomous equations using the substitution

$$E(t)=A(t)\exp(ibt). \tag{2}$$

Inserting Eq. (2) into Eq. (1), the factor $\exp(ibt)$ can be divided through as a consequence of the ϕ indeterminacy. The resulting system is again autonomous and has the form

$$\frac{dA}{dt}=(1+i\alpha)NA-ibA+\kappa\exp[-i(\omega_0\tau+b)]A(t-\tau),$$

$$T\frac{dN}{dt}=P-N-(1+2N)|A|^2. \tag{3}$$

We now have two equations (one complex and one real) in the complex variable $A(t)$ and the real variable $N(t)$, together with the unknown real parameter b. This form has the advantage that the ECMs, which are periodic solutions of Eq. (1), can be calculated as steady state solutions of Eq. (2) for an appropriately chosen value of b. From now on, we will call these types of solutions as *steady state solutions*. Similarly, quasiperiodic solutions (periodic intensity) of Eq. (1) can be calculated as periodic solutions of Eq. (2). We call them *periodic solutions*.

But the substitution (2) introduces another indeterminacy into the equations. Indeed, if $(A(t),N(t),b)$ is a solution of Eq. (3), then $(A^*(t),N^*(t),b^*)$ with

$$A^*(t)=\exp[i(b-b^*)t]A(t),$$

$$N^*(t)=N(t), \tag{4}$$

and $b \neq b^*$ being an arbitrary real number, is also a solution of Eq. (3), corresponding to the same solution $(E(t),N(t))$ of Eq. (1). We call this the b indeterminacy.

It is important to note that the (asymptotic) stability of a solution $(A(t),N(t),b)$ under Eq. (3) is the same as the stability of the corresponding solution $(E(t),N(t))$ under Eq. (1). Indeed, for fixed b, there is a one-to-one correspondence between the solutions of both equations. An (un)stable perturbation for a solution of one equation will therefore be transformed in an (un)stable perturbation for the corresponding solution of the other equation.

A. Steady state solutions

To compute ECMs as steady state solutions of Eq. (2), we require $A(t)=A_s$ and $N(t)=N_s$ to be constants. This is only possible for one particular choice of the parameter b, $b=b_s$. Hence, in this case the b indeterminacy is resolved and b_s is an extra unknown to be determined. The ϕ indeterminacy is removed by fixing the phase of A_s, e.g., using $\mathrm{Im}(A_s)=0$. Inserting $A_s=x_s+iy_s$ into Eq. (3) leads to the following nonlinear system for the (x_s,y_s,N_s,b_s):

$$\begin{bmatrix} N_s x_s+(b_s-\alpha N_s)y_s \\ +\kappa\cos[(\omega_0+b_s)\tau]x_s \\ +\kappa\sin[(\omega_0+b_s)\tau]y_s \end{bmatrix}=0,$$

$$\begin{bmatrix} (\alpha N_s-b_s)x_s+N_s y_s \\ -\kappa\sin[(\omega_0+b_s)\tau]x_s \\ +\kappa\cos[(\omega_0+b_s)\tau]y_s \end{bmatrix}=0,$$

$$P-N_s-(1+2N_s)(x_s^2+y_s^2)=0,$$

$$y_s=0. \tag{5}$$

B. Periodic solutions

Quasiperiodic solutions of Eq. (1) which emanate from the ECMs from Hopf bifurcation points, have the form $(A(t)\exp(ib_p t),N(t))$ with $A(t)=A(t+T_p)$ and $N(t)=N(t+T_p)$ for all t, where T_p is a positive real number. Therefore, they can be computed as periodic solutions $(A_p(t),N_p(t),b_p)$ of Eq. (3) with period T_p. Here, the requirement for $A_p(t)$ to be periodic restricts the possible values for b^* in Eq. (4). They are given by

$$b^*=b_p+n\frac{2\pi}{T_p}, \tag{6}$$

where n is an arbitrary integer. Hence, the continuous b indeterminacy is reduced to a discrete one, which does not pose numerical problems (see below).

To remove the ϕ indeterminacy, we introduce an extra condition analogous to the one used for the classical phase indeterminacy of periodic solutions [30]. When $u(t;0,0)=(A(t),N(t))$ is a periodic solution, then so is

$$u(t;\sigma_1,\sigma_2)=(A(t+\sigma_1)\exp(i\sigma_2),N(t+\sigma_1)) \tag{7}$$

for any real σ_1 and σ_2. Here, σ_1 presents a classical phase shift in time, while σ_2 presents a shift in the ϕ indeterminacy. Although theoretically various phase conditions can be imposed, an appropriate choice improves the robustness and the speed of the numerical calculations. Therefore, we use a phase condition that minimizes the distance between the solution $u(t;\sigma_1,\sigma_2)$ to be computed and $u_0(t)$, the initial approximation of the solution, i.e., we minimize

$$D(\sigma_1,\sigma_2)\equiv\int_0^{T_p}\|u(t;\sigma_1,\sigma_2)-u_0(t)\|^2 dt. \tag{8}$$

The optimal solution satisfies $\partial D/\partial\sigma_1=0$ and $\partial D/\partial\sigma_2=0$. This leads to the conditions

$$\int_0^{T_p}[\mathrm{Re}(\overline{A_0'(t)}A(t))+N_0'(t)N(t)]dt=0,$$

$$\int_0^{T_p}\mathrm{Im}(\overline{A_0'(t)}A(t))dt=0, \tag{9}$$

where the primes mean differentiation and a bar means the complex conjugate. Numerical continuation of branches of periodic solutions using the phase conditions (9) proved to be reliable, while the use of other phase conditions often produced false turning points (i.e., the continuation turns back on another representation of the computed branch at places where the branch itself does not turn).

Inserting $A(t)=x(t)+iy(t)$ into Eq. (3), we obtain the following nonlinear system for a periodic solution $(x_p(t),y_p(t),N_p(t),b_p,T_p)$:

$$\frac{dx_p}{dt}=N_p x_p+(b_p-\alpha N_p)y_p+\kappa\cos[(\omega_0+b_p)\tau]x_p(t-\tau)+\kappa\sin[(\omega_0+b_p)\tau]y_p(t-\tau),$$

$$\frac{dy_p}{dt}=(\alpha N_p-b_p)x_p+N_p y_p-\kappa\sin[(\omega_0+b_p)\tau]x_p(t-\tau)+\kappa\cos[(\omega_0+b_p)\tau]y_p(t-\tau),$$

$$T\frac{dN_p}{dt}=P-N_p-(1+2N_p)(x_p^2+y_p^2),$$

$$x_p(t)=x_p(t+T_p),$$

$$y_p(t)=y_p(t+T_p),$$

$$N_p(t)=N_p(t+T_p),$$

$$\int_0^{T_p}[x_0'(t)x(t)+y_0'(t)y(t)+N_0'(t)N(t)]dt=0,$$

$$\int_0^{T_p}(x_0(t)y(t)-y_0(t)x(t))dt=0. \tag{10}$$

Note that the resulting value of b_p, satisfying the periodicity condition, depends on the starting value chosen in the Newton process to solve the system (10).

III. A ONE-PARAMETER STUDY

In this section, we construct a detailed bifurcation diagram using the DDE-BIFTOOL software package [15,17] with the feedback strength κ as the bifurcation parameter. We used the feature of DDE-BIFTOOL to introduce extra free parameters and corresponding extra conditions, in order to cope with the nonuniqueness of solutions due to the ϕ indeterminacy. We use the same parameter values as in Ref. [13], i.e.,

$$P=0.001, \quad T=\tau=1000, \quad \alpha=4, \quad \omega_0\tau=-1. \quad (11)$$

These values correspond to a distance of 15 cm between the laser and the mirror. For reasons of comparison, however, it should be noted that Hohl and Gavrielides used $\omega_0\tau=-1.45$ to obtain their bifurcation diagram [31].

A. Steady state solutions

The ECMs are steady state solutions of Eq. (3) and can be computed analytically. Indeed, after eliminating y_s, N_s, and x_s^2 from Eq. (5), we obtain

$$b_s=-\kappa\{\alpha\cos[(\omega_0+b_s)\tau]+\sin[(\omega_0+b_s)\tau]\}. \quad (12)$$

The solutions of this transcendental equation in b_s together with

$$N_s=-\kappa\cos[(\omega_0+b_s)\tau],$$

$$x_s^2=\frac{P-N_s}{1+2N_s}, \quad (13)$$

correspond to the steady basic solutions of Eq. (1) whenever $x_s^2\geqslant 0$.

The electric field amplitude as a function of κ is plotted in Fig. 1. There is only one solution for $\kappa=0$, which corresponds to the solitary laser (therefore called the solitary mode). Increasing the feedback strength κ, new solutions appear in pairs through saddle-node bifurcations. By recomputing these branches of steady state solutions using the DDE-BIFTOOL software, we can determine their stability properties, see Fig. 1. The solitary mode is initially stable and changes stability at a Hopf bifurcation point. Furthermore, some of the upper branches, called modes, are initially stable and destabilize through Hopf bifurcation points, just like the solitary mode. The lower branches, called antimodes, are everywhere unstable. An exception is the branch which starts at zero amplitude and which is entirely unstable. This branch corresponds to a mode, of which the stable part and the corresponding antimode were eliminated by the condition $x_s^2\geqslant 0$. Note that on the mode and antimode branches a lot of additional Hopf bifurcations occur. Approximations of the first Hopf bifurcation points on the mode branches can be determined analytically [12,19] or by using simulations. The unstable Hopf bifurcation points have never been found before. In the following section, we show that these bifurcations play a role in understanding the dynamics of the laser.

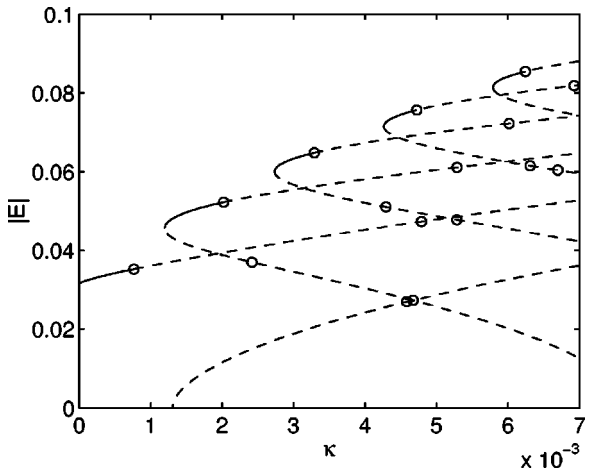

FIG. 1. Bifurcation diagram of the steady state intensity solutions. The figure represents the field amplitude $|E|$ vs the feedback rate κ. The values of the fixed parameters are given in Eq. (11). Full and dashed lines correspond to stable and unstable solutions, respectively. Circles indicate Hopf bifurcations. All upper branches undergo a change of stability through a Hopf bifurcation. Other Hopf bifurcations appear on the unstable branches.

B. Periodic solutions

Solutions of Eq. (1) with a time-periodic intensity of the field and their stability were computed using the collocation procedure implemented in DDE-BIFTOOL. During computations we used piecewise polynomials of degree 3 or 4 on (nonequidistant) meshes with 18–50 subintervals. Branches were started from the Hopf bifurcations found above.

Figure 2 shows these solutions in the $\max|E|$ vs κ plane. These branches exhibit an interesting structure. Each branch that starts at a destabilizing Hopf bifurcation on a mode increases in amplitude, undergoes some bifurcations, decreases in amplitude, and ends at a Hopf bifurcation on an antimode. In this way, different external cavity modes are connected. Hence, these connections are suggestive of a beating phenomena between mode and the antimode. This phenomenon has been suspected for some time [34,35] and was substantiated analytically in Ref. [19]. Numerical evidence of such a connection, however, came only recently because the connecting branch ends at an unstable Hopf point on an antimode, which can only be found via a continuation of unstable solutions. We will come back to this interpretation in Sec. IV B. This type of connection between modes and antimodes seems to be present in a generic way as more mode-antimode pairs appear. For instance, branches starting from Hopf points on modes always go to the right, while those starting from Hopf points on antimodes go to the left. The periodic solutions that start at the first Hopf point on a stable ECM are of particular interest, because they can be observed experimentally. Along each of these branches of periodic solutions, the stability evolves in a similar way. At some point of the branch, two Floquet multipliers leave the unit circle, and a torus bifurcation occurs.

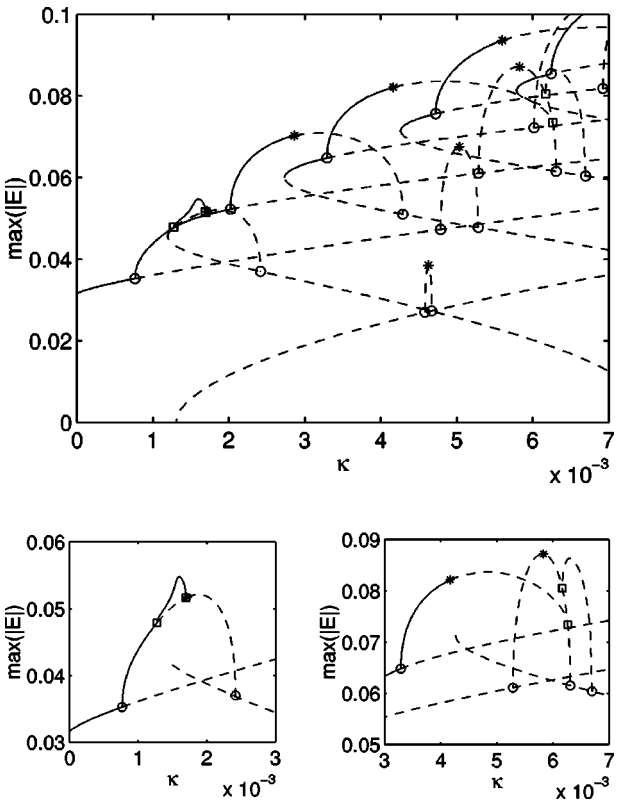

FIG. 2. Top: Bifurcation diagram of the steady state and periodic solutions. The figure represents the max$|E|$ vs the feedback parameter κ. Same values of the parameters as in Fig. 1. Full and dashed lines represent stable and unstable solutions, respectively. Hopf, torus, and period doubling bifurcation points are indicated by circles, stars, and squares, respectively. Bottom: Blow up of parts of the diagram clarifying the branching behavior of some of the periodic solutions. In the left figure, a first period-doubling bifurcation point leads to a branch of periodic solutions that terminates at a second period doubling bifurcation point located slightly below a torus bifurcation point. A very small domain of stable periodic solutions thus exists between the second period doubling bifurcation point and the torus bifurcation point. However, the torus bifurcation point marks the real change of stability of the bridge, as we may see for the other upper branches.

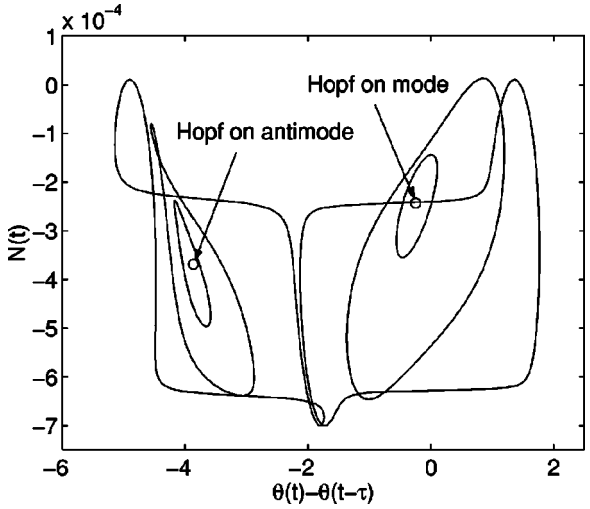

FIG. 3. Phase plane projection of some trajectories on the first mode-antimode connection. If $E=R\exp(i\theta)$, we represent the carrier density $N(t)$ as a function of $\theta(t)-\theta(t-\tau)$. The different trajectories correspond to $\kappa=0.77\times10^{-3}$ (Hopf on mode), $\kappa=0.81\times10^{-3}$, $\kappa=1.42\times10^{-3}$, $\kappa=1.84\times10^{-3}$, $\kappa=1.87\times10^{-3}$, $\kappa=2.18\times10^{-3}$, $\kappa=2.38\times10^{-3}$, and $\kappa=2.42\times10^{-3}$ (Hopf on antimode). As we progressively increase κ, the periodic orbits first encircle the mode and then the antimode.

On some branches additional bifurcations occur. For example, the branch that originates from the first Hopf bifurcation on the solitary mode, undergoes two additional period-doubling bifurcations. The period-doubled branch is entirely stable and quickly returns to the period-1 branch, just before a torus bifurcation destabilizes this branch. We will see in Sec. V how the first mode-antimode connection undergoes further changes as $\omega_0\tau$ is varied. (The bifurcation diagram in Ref. [13] additionally has a period-4 branch due to the different value for $\omega_0\tau$.)

Figure 3 shows the evolution of the first mode-antimode connection in a projection of the phase plane. Here, θ is the angle in the polar representation of the complex electrical field. Note that for steady state solutions, $\theta(t)-\theta(t-\tau)=b_s\tau$. Starting at the Hopf point on the mode, the branch grows, flips over to the right, and shrinks to the Hopf point on the antimode. On each branch of periodic orbits, there is one orbit that passes through the origin in the complex plane of the electric field. This explains the flip in Fig. 3 where one side of the projected orbit is discontinuously shifted by a phase difference of 2π. As another consequence, when continuing the branch from both sides, the profiles match only if one takes the (discrete) b indeterminacy into account.

IV. INFLUENCE OF THE LINEWIDTH ENHANCEMENT FACTOR

To determine if the bifurcation bridges that connects pairs of ECM are generic bifurcation features of the LK equations, we shall investigate how they vary in terms of two important physical parameters, namely, the linewidth enhancement factor α and the phase factor $\omega_0\tau$. We first consider the effect of α. Of particular physical interest is to determine how the stability of the bifurcation bridges change with α and how robust they are.

A. Two-parameter bifurcation sets

Specifically, we investigate the first bridge of periodic solutions ($0<\kappa\leqslant3\times10^{-3}$) as α is changed between 2 and 6. The values of the other parameters are documented in Ref. [13], see Eq. (11). Three distinct bifurcations appear, which we analyze separately.

Steady state bifurcations. Figure 4 shows the stability regions for the ECMs. The leftmost gray area indicates where the solitary mode is stable. The other two gray areas correspond to parameter values where the next upper ECM branches in Figs. 1 and 2 are stable. These areas are bordered by a curve of saddle-node bifurcations (to the left) and a curve of Hopf bifurcations (to the right). For the parameter values considered, one mode is always stable at a given

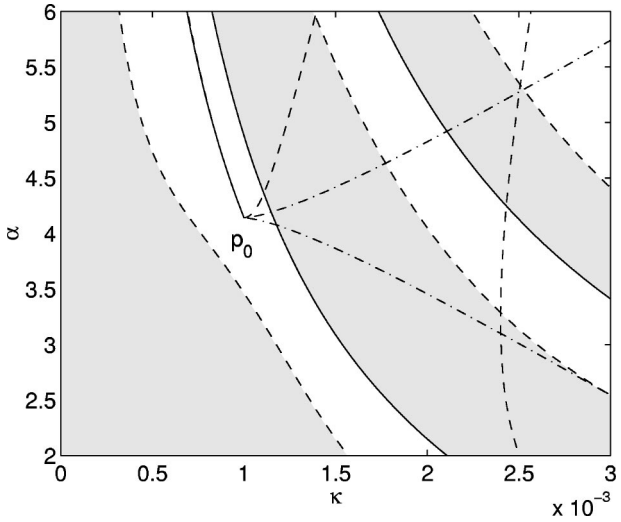

FIG. 4. Stability diagrams of the ECMs in the α vs κ diagram. Gray colored regions correspond to parameter values where an ECM is stable. Saddle-node bifurcation (or limit point) curves are shown by full lines. They mark the creation of pairs of mode-antimode solutions. The broken lines denote the Hopf bifurcation and the dashed broken lines the pitchfork bifurcation points. Point p_0 is a degenerate bifurcation point.

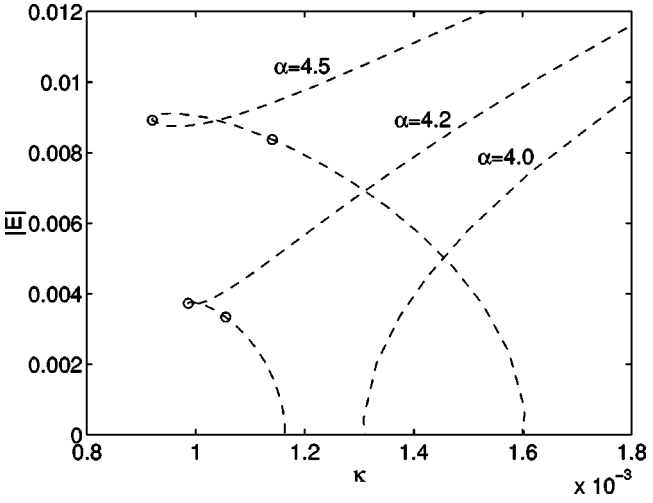

FIG. 5. Bifurcation diagram of steady state solutions for different values of α close to $\alpha_0 \simeq 4.14$. We represent $|E|$ vs κ for $\alpha = 4$, 4.2, and 4.5. Stable and unstable branches are shown by full and dashed lines, respectively (for $\alpha = 4.2$ and 4.5, there is a very small region of stability between the steady limit point and the Hopf bifurcation point near $\kappa = 1$, not shown). Hopf bifurcation points are marked by circles. Note the creation of the left steady limit point and the two Hopf bifurcation points as $\alpha > \alpha_0 \simeq 4$.

value of κ (the maximum gain mode [32]). The dashed curve that starts at $(\alpha,\kappa) = (2, 2.5\times10^{-3})$ is the curve of Hopf points on the antimode of the first ECM.

Five more curves are shown emanating from the point p_0. Going counterclockwise around p_0, these curves are respectively two curves, of steady pitchfork bifurcations, two Hopf curves and a saddle-node curve (note that one of the Hopf curves almost coincides with the saddle-node curve). By taking into account its properties, we find that p_0 is located at $(\kappa,\alpha) = (\kappa_0,\alpha_0)$, where

$$\kappa_0 = \tau^{-1} = 10^{-3} \quad \text{and} \quad \alpha_0 = \pi - \omega_0\tau \simeq 4.14. \tag{14}$$

See Sec. V A for more details on this point. Figure 5 shows the emergence of the Hopf and limit points as α passes the value α_0.

Periodic bifurcations. Two of the Hopf bifurcation curves shown in Fig. 4 are redrawn in Fig. 6. They are the first Hopf bifurcation on the solitary mode and the first Hopf bifurcation on the antimode of the first mode-antimode pair. These two points are connected by a branch of periodic solutions, as explained in the preceding section. The stability of these periodic solutions is lost at period doubling or torus bifurcation points. Curves of these bifurcations are also shown in Fig. 6. If α decreases, the period-doubling bifurcations disappear. If α increases, the torus bifurcation point merges with the rightmost period-doubling bifurcation.

Typical bifurcation diagrams of the steady and periodic solutions are shown in Fig. 7. If $\alpha = 3$, we observe the simplest bridge. The bridge connects a mode and an antimode and undergoes a torus bifurcation. If $\alpha = 3.6$, a period-2 branch appears. After the torus bifurcation has disappeared by merging with the rightmost period-doubling bifurcation point ($\alpha \simeq 4.1$), the period-doubled branch starts to fold and additional period-doubling bifurcations occur. For larger α, the period-4 branch follows a similar scenario possibly leading to a period-doubling cascade. For $\alpha = 6$, the bridge breaks and includes homoclinic and period-doubling bifurcations between the two Hopf points.

The breaking phenomenon shown in Fig. 7 for $\alpha = 6$ follows a complicated Shil'nikov-type scenario (Fig. 8). Between $\alpha = 5.2$ and $\alpha = 5.3$, the period-2 branch is intersected by a branch of homoclinic trajectories. Between $\alpha = 5.3$ and $\alpha = 5.4$, an isolated branch of periodic solutions merges to the left with the period-1 branch and to the right with the period-2 branch, via a period-doubling bifurcation. For α

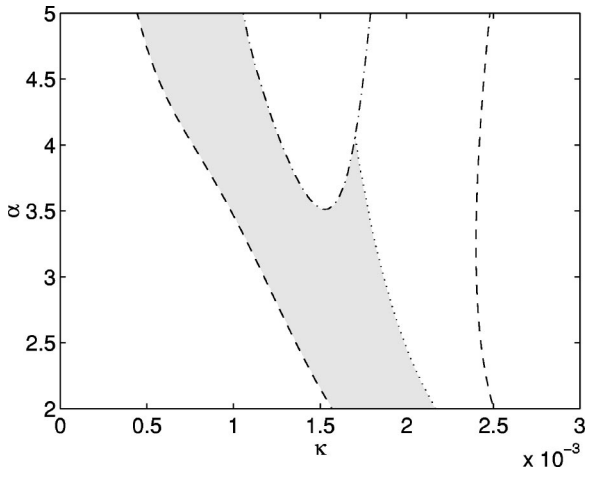

FIG. 6. Stability diagram of the first bifurcation bridge. The gray region indicates the stability region in the α vs κ diagram. Hopf, period-doubling, and torus bifurcation points are shown by broken, broken dashed, and dashed lines, respectively.

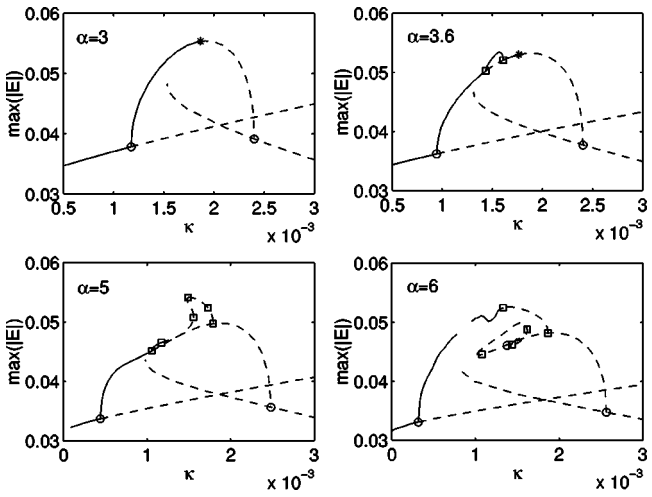

FIG. 7. Bifurcation diagram of the steady and periodic solutions for selected values of α. Each figure represents max$|E|$ vs κ. From left to right and from top to bottom, the figures correspond to $\alpha=3$, $\alpha=3.6$, $\alpha=5$, and $\alpha=6$. Stable and unstable branches are shown by full and dotted lines, respectively. Hopf, torus, and period-doubling bifurcation points are shown by circles, stars, and squares, respectively.

$\simeq 5.8$, another branch of homoclinic trajectories intersects the period-1 branch.

Homoclinic trajectories can play a prominent role in the global dynamics. We approximate these trajectories by periodic solutions with large period, i.e., $T_p \gg \tau$. Figure 9 shows two phase plane projections, together with the ECMs that are present in the system for these parameter values. The first homoclinic solution involves an antimode with two unstable complex conjugated eigenvalues, the second one involves a mode with one unstable real eigenvalue. The former homoclinic is of Shil'nikov type, as indicated in Fig. 10, which reveals the typical oscillatory behavior of the period over the branch of periodic solutions approaching the homoclinic orbit.

B. Different types of dynamical behavior

The gradual complexity of the bifurcation diagram as α increases is consistent with experimental studies [20,21] where lasers with different α have been tested. In the preceding section, we showed that a bifurcation bridge connecting two distinct modes progressively deteriorates as α approaches $\alpha=6$. The bridge undergoes period-doubling bifurcations and breaks through homoclinic orbits. The disappearance of the original bridge is also noticed by the time traces and associated spectra. See Figs. 11 and 12.

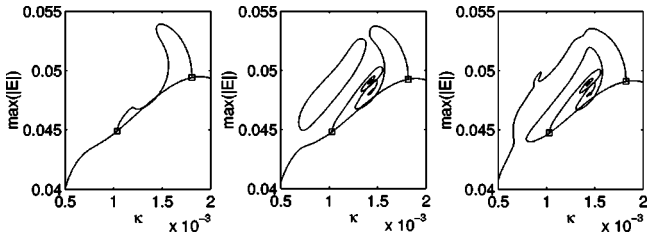

FIG. 8. The progressive folding of the period-2 branch. We represent max$|E|$ vs κ for the first bridge. From left to right, the three figures correspond to $\alpha=5.2$, $\alpha=5.3$, and $\alpha=5.4$, respectively. For clarity, stability is not indicated. Period-doubling bifurcation points are shown by squares.

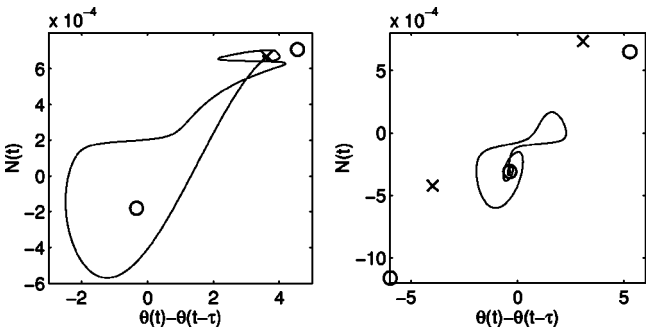

FIG. 9. Homoclinic orbits. Phase plane projection of two periodic orbits exhibiting very large period ($T_p=10^5 \gg \tau=10^3$). Left: $\kappa \simeq 7.7\times10^{-4}$ and $\alpha=6$. The figure represents ECMs [mode (○), antimode (×)] and a homoclinic orbit ending the left branch of periodic solutions in Fig. 7. Right: $\kappa \simeq 1.52\times10^{-3}$ and $\alpha=6$. The figure represents ECMs [mode (○), antimode (×)] and the homoclinic solution that is ending the right branch of periodic solutions in Fig. 7.

For $(\alpha,\kappa)=(4,10^{-3})$, the laser intensity of the field is almost harmonic, as can be seen in the optical spectrum. The right peak corresponds to the frequency at the Hopf point on the mode, and the left peak corresponds to the frequency at the Hopf point on the antimode. Therefore, the two peaks can be interpreted as mode and antimode frequencies. The rf spectrum, which basically consists of one ac peak, is then understood as the beating frequency between mode and antimode. This is consistent with an asymptotic analysis of the LK equations for large values of T [19]. For larger α, however, the frequency content of the intensity oscillations is much richer. Other peaks, not associated with mode or anti-

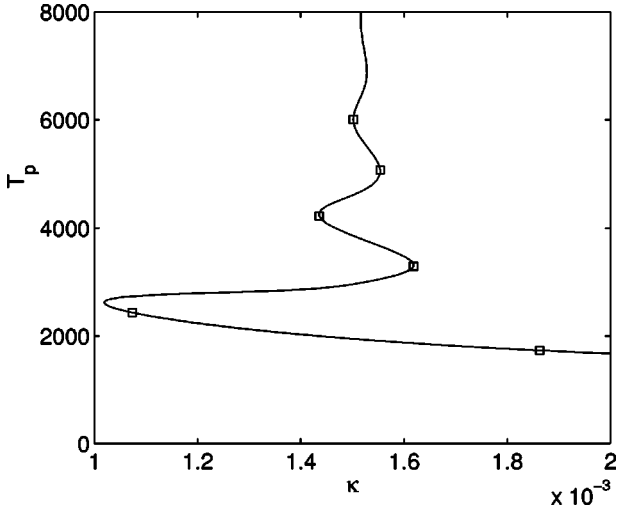

FIG. 10. Shil'nikov bifurcation scenario. The figure represents the period along a branch of periodic solutions approaching a homoclinic orbit of Shil'nikov type. $\alpha=6$, and stability is not indicated. The period-doubling bifurcation points are shown by squares.

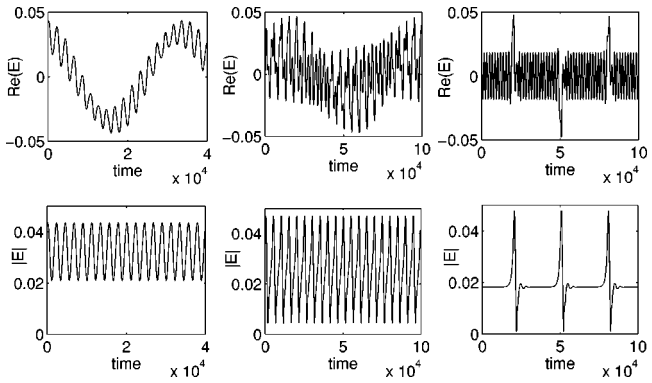

FIG. 11. Time traces for periodic solutions located on the first bridge. From left to right: $(\alpha,\kappa)=(4,10^{-3})$, $(\alpha,\kappa)=(6,7\times10^{-4})$, and $(\alpha,\kappa)=(6,7.7\times10^{-4})$. Top: real part of E. Bottom: field amplitude $|E|$.

mode, can dominate the spectra. Close to a homoclinic solution, where the spectrum becomes large, the spectrum becomes almost continuous. The ECM that belongs to the homoclinic trajectory appears very clearly, see Fig. 12 (right, top). Note that such low-frequency peaks are of a different nature than those that appear in the LFF regime.

V. CHANGING THE FEEDBACK PHASE

The feedback phase $\omega_0\tau$ is an interesting parameter because it dramatically changes the relative positions of the ECMs (see, for example, the bifurcation diagrams in Fig. 15 of Ref. [1]). In this section we investigate the solutions of the LK equations for $0<\kappa\leqslant 3\times10^{-3}$ and for $-\pi\leqslant\omega_0\tau\leqslant\pi$. The other values of the parameters remain fixed and are documented in Ref. [13], see Eq. (11).

A. Steady state solutions

Figure 13 represents the stability diagram of the steady state solutions. The gray area indicates the regions where a mode is stable. Such a region is located between a saddle-

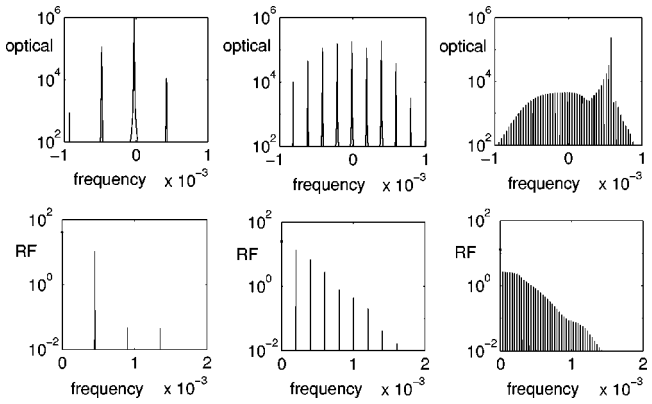

FIG. 12. Spectra of time traces shown in Fig. 11. From left to right: $(\alpha,\kappa)=(4,10^{-3})$, $(\alpha,\kappa)=(6,7\times10^{-4})$, and $(\alpha,\kappa)=(6,7.7\times10^{-4})$. Top: optical spectrum. Bottom: rf spectrum. Note that the rightmost case corresponds to a periodic solution with a large period, close to a homoclinic bifurcation.

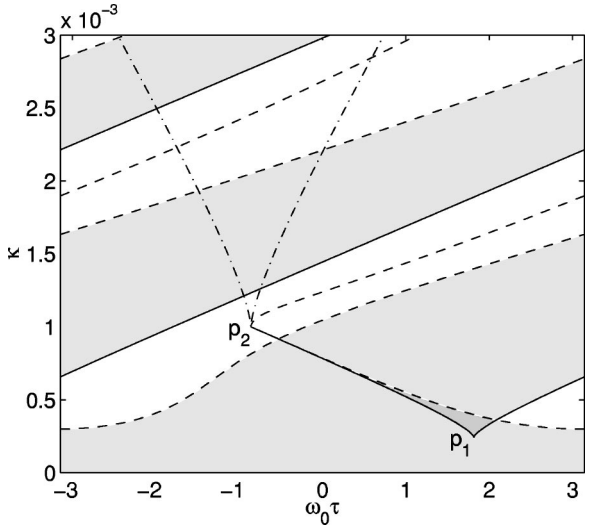

FIG. 13. Stability diagram of the ECMs in the κ vs $\omega_0\tau$ plane. Light and dark gray regions mean one stable ECM and two stable ECMs, respectively. Saddle-node, Hopf, and pitchfork bifurcations are shown by full, broken, and dashed-broken lines, respectively.

node curve and a Hopf curve. The curve of the first Hopf bifurcation on an antimode (dashed line) is located in between these stable zones. The diagram shows that as a mode-antimode pair is continued in the parameter $\omega_0\tau$ over a distance of 2π, we arrive at the next mode-antimode pair. In this way, the connecting branch of periodic solutions which we presented in the previous sections is transported from one pair of ECMs to the next by simply changing the feedback phase. This explains why the structure of the different bridges, see Fig. 2, is so similar.

In a small region of parameter space, two modes are stable for the same parameter values. The branch of saddle-node bifurcations, which delimits this region, has a cusp at p_1. Analytically, it can be shown [33] that the point p_1 lies at

$$\omega_0\tau=\pi-\arctan(\alpha)\simeq1.816, \tag{15}$$

$$\kappa=\frac{1}{\tau\sqrt{1+\alpha^2}}\simeq2.43\times10^{-4}. \tag{16}$$

Moreover, the ECM frequency $b_s\tau=0$ at that point.

The saddle-node curve ends at the point p_2, together with several other curves, i.e., two Hopf curves and two curves of pitchfork bifurcations. Along these curves, the intensity of the laser field goes to zero when approaching p_2, which allows its analytical determination. Note that the point p_0 in Fig. 4 is of the same nature as point p_2, and can be determined in a similar way.

To determine the values of b_s, $\omega_0\tau$, and κ at p_2, we need three conditions. A first condition is given by Eq. (12) for the ECM frequency. At point p_2, a mode and an antimode are created. This implies a double zero of Eq. (12). From the condition $d\kappa/db_s=0$, we obtain

$$\tau^{-1}=\kappa\{\alpha\sin[(\omega_0+b_s)\tau]-\cos[(\omega_0+b_s)\tau]\}. \tag{17}$$

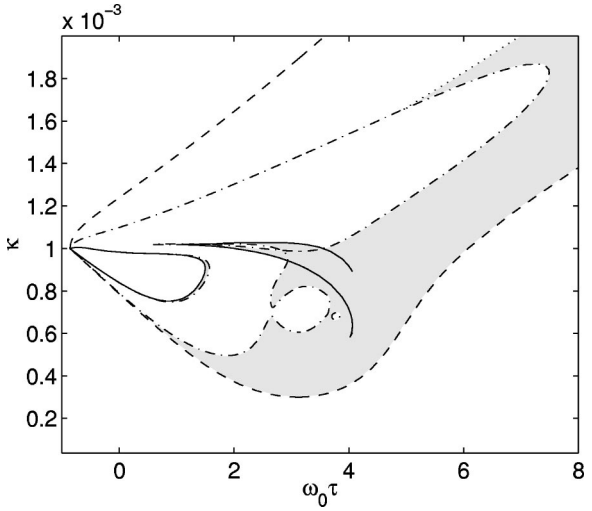

FIG. 14. Stability diagram of periodic solutions in the κ vs $\omega_0\tau$ plane. The gray region corresponds to parameter values where the periodic solutions on the first bridge are stable. Saddle node of periodic solutions, Hopf, period-doubling, and torus bifurcations are represented by full, broken, dashed broken, and dashed lines, respectively.

Since the mode-antimode pair has zero field intensity, $x_s^2=0$, from Eq. (13) we determine a third condition

$$P+\kappa\cos[(\omega_0+b_s)\tau]=0. \tag{18}$$

Equations (12), (17), and (18) are three equations for $b_s, \omega_0\tau$, and κ. Note that our parameter values listed in Eq. (11) verify the relation

$$P=\tau^{-1}, \tag{19}$$

and implies from Eqs. (17) and (18) that $(\omega_0+b_s)\tau=n\pi$ where n is an integer. The point p_2 in Fig. 13 corresponds to $n=1$, and is located at

$$\omega_0\tau=\pi-\alpha\simeq-0.858, \quad \kappa=\tau^{-1}=10^{-3}. \tag{20}$$

The critical ECM frequency is given by $b_s\tau=\alpha$. At the point p_2, the characteristic equation has four zero characteristic roots. But p_2 is not a generic point. If the particular condition (19) is not verified, the point where the mode-antimode pair appears with zero field intensity does no longer fall on a branch of Hopf bifurcations.

B. Periodic solutions

The point p_2 at $\omega_0\tau\simeq-0.86$ and $\kappa=10^{-3}$ is not only the end point of curves of saddle node and Hopf bifurcations, but also the end point of several curves of bifurcation points on periodic solution branches. This is shown in Fig. 14 where for the sake of clarity, the parameter $\omega_0\tau$ is drawn without the mod(2π) operation. Besides the two Hopf bifurcation curves that delimit the first connecting branch of periodic solutions, branches of period-doubling bifurcations, saddle-node bifurcations (for periodic solutions), and homoclinic trajectories (not shown) start at the point p_2. For increasing

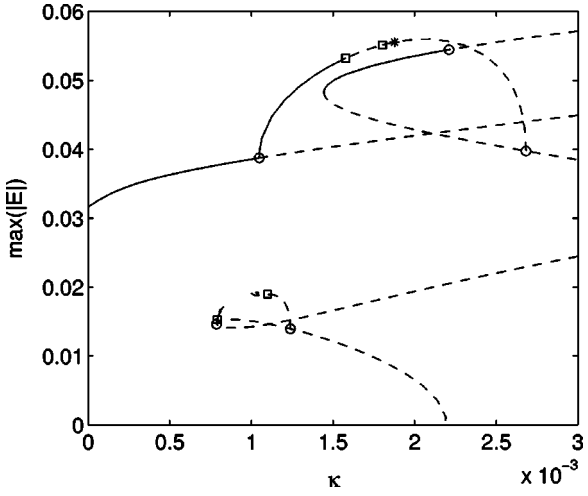

FIG. 15. Bifurcation diagram of the periodic solutions; max$|E|$ is represented as a function of κ for the first bridge and $\omega_0\tau=0$. Stable and unstable branches are represented by full and broken lines, respectively. Hopf, torus, and period-doubling bifurcation points are shown by circles, stars, and squares, respectively.

$\omega_0\tau$, these branches turn, merge, and split again to form a complicated bifurcation diagram. Additional saddle-node bifurcations appear ($\omega_0\tau\simeq1$ and $\omega_0\tau\simeq4.1$) and disappear again by splitting off an isolated branch of periodic solutions ($\omega_0\tau\simeq4.2$). For larger $\omega_0\tau$, the diagram becomes comparable to Fig. 6.

How these different bifurcation curves contribute to the dynamical behavior can be seen in Figs. 15–17. For five values of $\omega_0\tau$, a bifurcation diagram in the parameter κ is shown. To the right of and close enough to the point p_2, the branches of periodic solutions, which are born at the Hopf points, do not connect but tend to homoclinic trajectories from both sides. Compare, for instance, the situation at $\omega_0\tau=0$ in Figs. 14 and 15 (lower part), where there is no connection yet, to the situation at $\omega_0\tau=2\pi$ in Figs. 14 and 15 (upper part). The transition between these situations happens basically in two steps.

First the two periodic branches glue together (at $\omega_0\tau\simeq1.5$, see Fig. 16). Then, a branch of periodic solutions connecting the two homoclinic trajectories, a branch that connects a Hopf point on a mode, and a Hopf point on an antimode are obtained. This connection is in many aspects similar to those encountered before, except that mode and

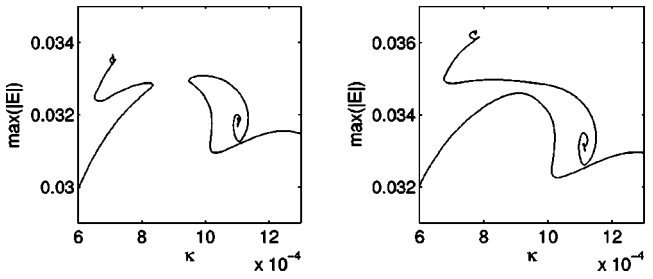

FIG. 16. Bifurcation diagram of the periodic solutions; max$|E|$ is represented as a function of κ. From left to right, $\omega_0\tau=1.4$ and $\omega_0\tau=1.6$. Stability is not indicated.

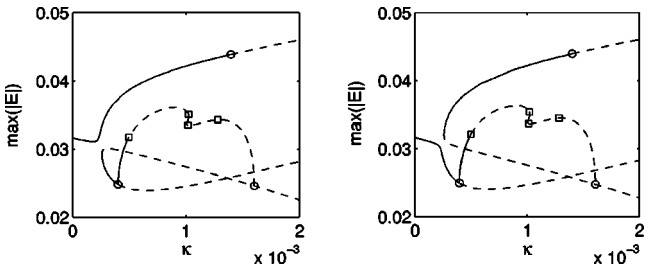

FIG. 17. Bifurcation diagram of the periodic solutions; $\max|E|$ is represented as a function of κ. From left to right, $\omega_0\tau=1.8$ and $\omega_0\tau=1.83$. Stable and unstable branches are represented by full and broken lines, respectively. Hopf, torus, and period-doubling bifurcation points are shown by circles, stars, and squares, respectively.

antimode belong to the same steady state branch.

Second, the steady state branch, which connects a mode and an antimode, glues to the branch with the solitary mode (between $\omega_0\tau=1.8$ and $\omega_0\tau=1.83$, see Fig. 17). As a result, the branch now connects a mode and an antimode from two different branches. This (steady state) branching behavior corresponds to the cusp in the branch of saddle-node bifurcations (point p_1 in Fig. 13).

For larger $\omega_0\tau$ (Fig. 14), the branch of periodic solutions loses its saddle-node bifurcations and middle period-doubling bifurcations. Further on, the two remaining period-doubling bifurcations are replaced by a torus bifurcation in a scenario similar to that of Sec. IV.

VI. CONCLUSION

In this paper we studied the Lang-Kobayashi equations for semiconductor lasers subject to optical feedback. Our study is based on the application of the numerical techniques implemented in the package DDE-BIFTOOL for stability and bifurcation analyses of delay differential equations. First, we showed how to exploit the symmetry properties of the equations to enable the computation of both basic solutions (solutions with constant field intensity) and solutions exhibiting pulsating intensities. Then, we carried out a detailed bifurcation analysis in the region of weak feedback. We showed and investigated the existence of branches of periodic solutions connecting mode and antimode branches. Such connections or bifurcation bridges have been suspected for some time, but could not be shown directly without a computation of both stable and unstable parts of solution branches. The basic phenomenon here corresponds thus to a beating between the two frequencies associated with mode and antimode. We further investigated the influences of the linewidth enhancement factor and feedback phase on the first mode-antimode bridge. This analysis reveals that increasing the linewidth enhancement factor progressively changes the stability of the bridge, but α must be high enough ($\alpha=6$) for rupture. Changing the feedback phase has a different effect on the bifurcation diagram. Because the feedback phase modifies the relative position of nearby ECMs, bifurcation bridges are also twisted. In addition to the mode-antimode connection between distinct branches, a mode-antimode connection is possible for the same branch of ECM solutions (see Fig. 17). For both the linewidth enhancement factor and the feedback phase, the mechanism for rupture of the connecting branch of periodic solutions is through homoclinic orbits.

ACKNOWLEDGMENTS

This research presents results of Grant No. OT 98/16 funded by the Research Council KU Leuven, of Grant No. G.0270.00 funded by the Fund for Scientific Research, Flanders (Belgium) and of the Research Project IUAP P4/02 and IUAP P4/07 funded by the program on InterUniversity Attraction Poles, initiated by the Belgian State, Prime Minister's Office for Science, Technology and Culture. B.H. and K.E. acknowledge the Fund for Scientific Research, Flanders (Belgium). T.E. acknowledges the FNRS (Fonds National de la Recherche Scientifique), the US Air Force Office of Scientific Research Grant No. AFOSR F49620-98-1-0400, and the National Science Foundation Grant No. DMS-9973203.

[1] G.H.M. van Tartwijk and D. Lenstra, J. Opt. B: Quantum Semiclassical Opt. **7**, 87 (1995).
[2] G.H.M. van Tartwijk and G.P. Agrawal, Prog. Quantum Electron. **22**, 43 (1998).
[3] *Fundamental Nonlinear Dynamics of Semiconductor Lasers*, edited by D. Lenstra, special issue of J. Opt. B: Quantum Semiclassical Opt. **9** (1997).
[4] *Nonlinear Laser Dynamics: Concepts, Mathematics, Physics, Applications*, edited by B. Krauskopf and D. Lenstra, AIP Conf. Proc. No. 548 (AIP, Melville, NY, 2000).
[5] G.H.M. van Tartwijk, A.M. Levine, and D. Lenstra, IEEE J. Sel. Top. Quantum Electron. **1**, 466 (1995).
[6] I. Fischer, G.H.M. van Tartwijk, A.M. Levine, W. Elsässer, E. Göbel, and D. Lenstra, Phys. Rev. Lett. **76**, 220 (1996).
[7] G. P. Agrawal and N. K. Dutta, *Long-wavelength Semiconductor Lasers* (Van Nostrand Reinhold, New York, 1986).
[8] H. Kawaguchi, *Bistabilities and Nonlinearities in Laser Diodes* (Artech House, Boston, 1994).
[9] T. Heil, I. Fischer, W. Elsässer, and A. Gavrielides, Phys. Rev. Lett. **87**, 243901 (2001).
[10] R. Lang and K. Kobayashi, IEEE J. Quantum Electron. **QE-16**, 347 (1980).
[11] P.M. Alsing, V. Kovanis, A. Gavrielides, and T. Erneux, Phys. Rev. A **53**, 4429 (1996).
[12] T. Erneux, Proc. SPIE **3944**, 588 (2000).
[13] A. Hohl and A. Gavrielides, Phys. Rev. Lett. **82**, 1148 (1999).
[14] D. Pieroux, T. Erneux, B. Haegeman, K. Engelborghs, and D. Roose, Phys. Rev. Lett. **87**, 193901 (2001).
[15] K. Engelborghs, DDE-BIFTOOL: a MATLAB package for bifurcation analysis of delay differential equations. Department of Computer Science, Report No. TW-305, 2000. Available from http://www.cs.kuleuven.ac.be/<koen/delay/ddebiftool.shtml

[16] K. Engelborghs, T. Luzyanina, K.J. in 't Hout, and D. Roose, SIAM J. Sci. Comput. (USA) **22**, 1593 (2000).
[17] K. Engelborghs, T. Luzyanina, and D. Roose, J. Comput. Appl. Math. **125**, 265 (2000).
[18] K. Engelborghs and D. Roose, Adv. Comput. Math. **10**, 271 (1999).
[19] T. Erneux, F. Rogister, A. Gavrielides, and V. Kovanis, Opt. Commun. **183**, 467 (2000).
[20] T. Heil, I. Fischer, and W. Elsässer, Phys. Rev. A **60**, 634 (1999).
[21] T. Heil, I. Fischer, and W. Elsässer, J. Opt. B: Quantum Semiclassical Opt. **2**, 413 (2000).
[22] A. Hohl and A. Gavrielides, Opt. Lett. **23**, 1606 (1998).
[23] M. Sciamanna, F. Rogister, O. Deparis, P. Mégret, M. Blondel, and T. Erneux, Opt. Lett. **27**, 261 (2002).
[24] M. Sciamanna, T. Erneux, F. Rogister, O. Deparis, P. Mégret, and M. Blondel, Phys. Rev. A **65**, 041801 (2002).
[25] T. Erneux, A. Gavrielides, and M. Sciamanna, Phys. Rev. A **66**, 033809 (2002).
[26] D. Pieroux and P. Mandel, Phys. Rev. E (to be published).
[27] K. Green and B. Krauskopf, Phys. Rev. E **66**, 016220 (2002).
[28] K. Green, B. Krauskopf, and K. Engelborghs, Physica D (to be published).
[29] B. Krauskopf, G.M.H. van Tartwijk, and G.R. Gray, Opt. Commun. **177**, 347 (2000).
[30] E.J. Doedel, H.B. Keller, and J.P. Kernevez, Int. J. Bifurcation Chaos Appl. Sci. Eng. **1**, 745 (1991).
[31] A. Hohl and A. Gavrielides (private communication).
[32] A.M. Levine, G.H.M. van Tartwijk, D. Lenstra, and T. Erneux, Phys. Rev. A **52**, R3436 (1995).
[33] G.A. Acket, D. Lenstra, A.J. Den Boef, and B.H. Verbeek, IEEE J. Quantum Electron. **20**, 1163 (1984).
[34] A.A. Tager and B.B. Elenkrig, IEEE J. Quantum Electron. **29**, 2886 (1993).
[35] A.A. Tager and K. Petermann, IEEE J. Quantum Electron. **30**, 1553 (1994).